Investigating Closed and Open Site Stability of Sn-, Ti-, Zr-, and Hf-Beta Zeolites: A Comprehensive Periodic-DFT Study

Nawras Abidi, Yacine Boudjema, Céline Chizallet, Kim Larmier

Investigating Closed and Open Site Stability of Sn-, Ti-, Zr-, and Hf-Beta Zeolites: A Comprehensive Periodic-DFT Study

Nawras Abidi, Yacine Boudjema, Céline Chizallet, and Kim Larmier*

IFP Energies nouvelles, Rond-point de l'échangeur de Solaize, BP3, 69360 Solaize, France

E-mail: kim.larmier@ifpen.fr

Abstract

This study presents a comprehensive periodic DFT analysis of Sn-, Ti-, Zr-, and Hf-doped Beta zeolites, materials known for their versatile catalytic properties in sustainable chemical processes. We focus on assessing the stability of closed versus open sites which is crucial to monitor the nature of the active sites under relevant conditions for analysis and catalysis. Using first-principles thermodynamics, we find that closed sites are stable under low water pressure and high temperature but over stability (T, P) domain that depend on the nature of the metal and on its location in the framework. Our findings also offer novel insights into water adsorption in zeolites with respect to earlier proposals by favoring scenarios with undissociated H_2O. The evaluation of Lewis acidity, quantified by pyridine adsorption, shows various acidity levels across different T sites, with T6 (following the polymorph B terminology) showing the strongest and T9 the weakest Lewis acidity. Titanium (Ti) is identified as having the weakest Lewis acidity among the studied dopants. A subtle interplay between electrostatic field and bonding energy terms is shown to be correlated with this behaviour. This study improves the molecular understanding of zeolite stability and catalytic behavior,

providing valuable insights for the development of advanced catalysts in sustainable chemical processes.

Keywords

Periodic DFT, zeolites, Sn-Beta, Ti-Beta, Zr-Beta, Hf-Beta, hydrolysis, Lewis acidity

1 Introduction

Since their initial identification in the 18th century by renowned Swedish mineralogist Axel Fredrik Cronstedt, zeolites have played a pivotal role in advancing the areas of adsorption and catalysis.[1] These unique crystalline microporous aluminosilicates are noted for their intricately arranged tetrahedral frameworks (T sites, where 'T' denotes the tetrahedral positions within the zeolite framework[2]), forming a complex lattice. This structure, marked by uniform micropore formations, is essential for efficient molecular sieving,[3,4] ion exchange,[5] and catalysis[6–10] establishing zeolites as critical components in a wide array of industrial applications.[11–14]

The integration of metals like Sn (Tin), Ti (Titanium), Zr (Zirconium) and Hf (Hafnium) into zeolite frameworks has been a breakthrough in catalysis and materials science.[8–10,15–17] These modified zeolites show exceptional catalytic abilities and stability, suitable for numerous advanced applications. Sn-zeolites, especially Sn-Beta, are notable for their superior catalytic performance in reactions such as glucose isomerization to fructose[18] and Baeyer-Villiger oxidations.[19] The creation of Lewis acidic sites by Sn integration is key to their high catalytic efficiency. Corma et al.[20,21] pointed the hydrophobic and oleophilic characteristics of Sn-zeolites, boosting their effectiveness in various organic transformations. Ti-containing zeolites, like Ti-Beta and Ti-Silicalite, excel in oxidation reactions, often employing hydrogen peroxide as an eco-friendly oxidant.[22,23] They play a crucial role in the epoxidation of olefins and hydroxylation of aromatics.[24,25] Zr- and Hf-zeolites, while less explored, show promising performances in processes such as alkane isomerization and cracking.[26,27]

Focusing on the metal insertion in T positions within zeolite frameworks, a considerable amount of research, both experimental and theoretical, has been conducted. Most of the experimental studies focused on Beta zeolites as a mixture of polymorphs A and B with Sn insertion. Bare et al.[28] synthesized Sn-Beta zeolite using the fluoride synthesis route. They identified the T5 and T6 sites in six-membered rings (following the terminology of the T sites of the polymorph A) as predominant locations for tin (Sn) in zeolite Beta by

Extended X-ray Absorption Fine Structure (EXAFS) spectroscopy, moving away from the earlier notion of random metal insertion demonstrated in the case of Ti-silicate-1.[29] If a T5 (or T6) site is occupied by Sn, the corresponding T5 (or T6) site on the opposite side of the six-ring is always occupied by Sn. Kolyagin et al.,[30] identified a distinct preference for Sn to occupy the T1 and T2 positions in the Sn-Beta zeolite framework. This observation was made for Sn-Beta zeolites synthesized using an alkaline hydrothermal synthesis method with a doped precursor approach. The study utilized advanced techniques such as EXAFS and ^{119}Sn Magic Angle Spinning Nuclear Magnetic Resonance (MAS NMR) to pinpoint the location of Sn within the zeolite structure.

From a theoretical point of view, studies have predominantly focused on polymorph A of the Beta zeolite. Wolf et al.,[31] Shetty et al.,[32] and Wang et al.,[33] by Density Functional theory (DFT) calculations, have provided valuable insights into Sn's favored sites within polymorph A confirming the stability of T1 and T2 substitution sites. In addition, the theoretical studies complement the experimental findings by offering detailed insights into heteroatom substitution including elements such as Ti, Sn, Hf, Zr, and Ge in different types of zeolites. Montejo-Valencia et al.,[34] using DFT calculations and periodic boundary conditions, delved into the Lewis acidities and hydrothermal stabilities of various zeolites, including polymorph A and C of the Beta zeolite, FAU and MFI, with Ti, Sn, and Ge. They quantify a preference for metal substitution at the T1 site in both polymorphs of Beta zeolite. In a related discovery,[35] this group identified that polymorph A of Sn-Beta zeolite, especially with double Sn-substitution, demonstrated the highest Lewis acidity compared to Sn in FAU, MFI and BEC and Ti in all the zeolites mentioned. Yang et al.[36] conducted in-depth investigations into the siting of Ti, Sn, and Zr heteroatoms in zeolite Beta (polymorph A) using periodic DFT calculations. Their results indicated a preference for introducing these heteroatoms at the T2 crystallographic position, with Sn- and Zr-substituted Beta zeolites exhibiting notably higher Lewis acidity than Ti-Beta. The adsorption of water has been used as a probe to evaluate the Lewis acidity of heteroatoms at different lattice sites of the

studied Beta zeolite. This study underscored the impact of the crystallographic location of heteroatoms on Lewis acidity and their interactions with water. Discrepancies in the literature regarding the most stable T site by theoretical studies may stem from variations in pseudopotentials (ultrasoft Vanderbilt vs. PAW) and dispersion corrections (DFT-D2 vs. DFT-D3).

The literature has also discussed the existence of two distinct types of sites within zeolites, commonly referred to as 'closed' or 'open' sites, each defined by its unique structural characteristics. As shown in Fig. 1, closed sites are identified by a tetrahedral geometry in which the metal is coordinated with four M-O-Si bonds. In contrast, open sites are characterized by at least partially hydrolyzed M-O-Si bonds, leading to the formation of M-OH bonds and nearby Si-OH groups.[37] This structural differentiation is known to significantly influence reactivity, with some studies suggesting that the proximity of Si-OH groups is crucial for stabilizing intermediates in specific reactions, such as the isomerization of glucose into fructose.[17,18,38,39] Furthering the understanding of open site configurations in Sn-Beta zeolites, To et al.[40] proposed based on earlier experimental findings on TS-1[41,42] and QM/MM calculations the coexistence of two distinct types of open sites (see Fig. 1): Syn configuration, when the SiOH group is adjacent to the SnOH group, and Anti configuration, where the SiOH group is positioned behind the SnOH instead - though this latter notion is referred to as "inversion" in the cited documents. Josephson et al.[43] later conducted an extensive DFT theoretical study where they explored the transformation of a tetrahedral Sn site into an open site. Their findings indicate enhanced stability of the Anti configuration compared to the Syn configuration, a finding supported by Bukowski et al.[44] (see Fig. 1). However, the focus on only Sn as dopant and the exclusion of non-dissociated water molecules in their analysis raised questions about the energetic relevance of these open sites, providing a nuanced view of the complex interactions within these zeolite structures.

To delineate the structure, activity, and specificity of close versus open active sites in Beta zeolites experimentally, techniques like NMR,[31,45–48] Infrared Spectroscopy (IR),[49–52]

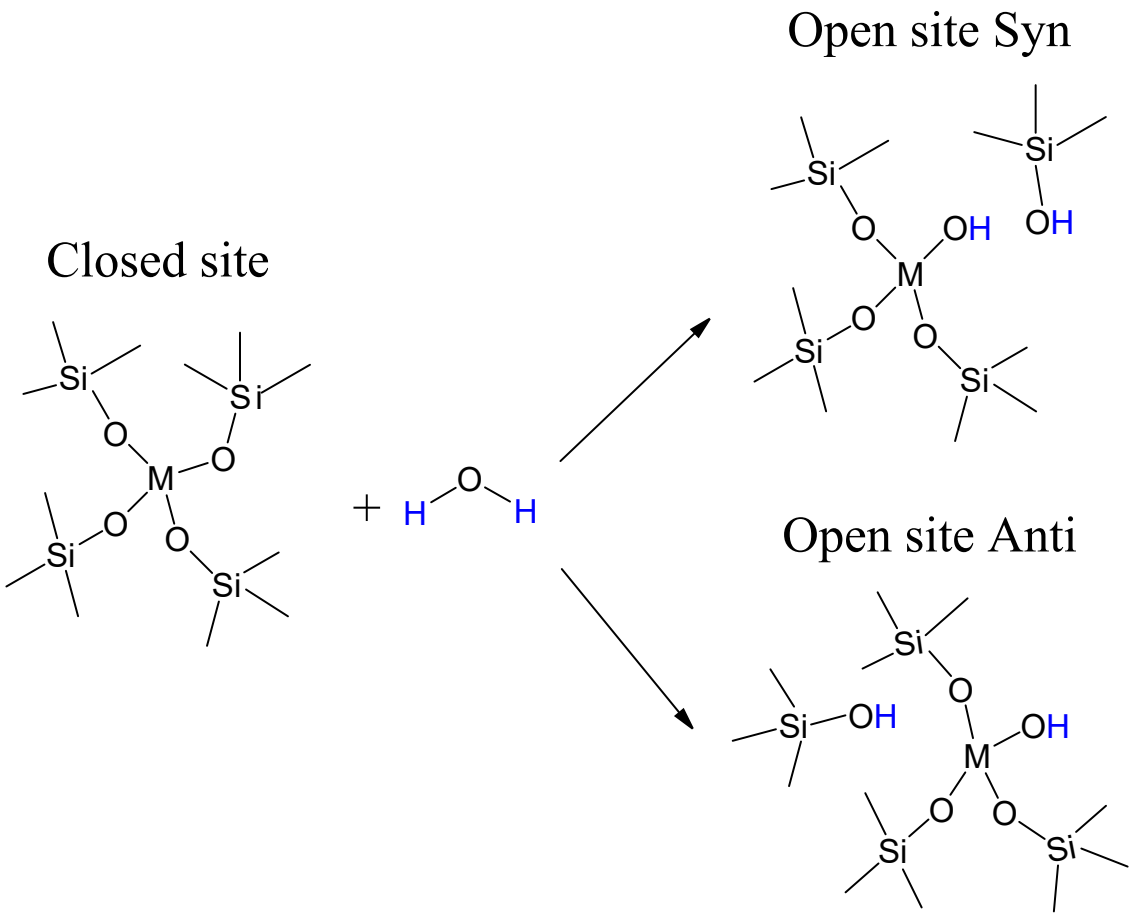

Figure 1: Hydration reaction of the metal substituted zeolite: transition from closed site characterized by a metal atom (M) coordinated with four framework oxygen atoms to an open site where the metal atom (M) holds hydroxyl groups (OH). The orientation of OH groups bonded to Si atoms determines the resultant Syn or Anti configuration of the open site.

X-ray Photoelectron Spectroscopy (XPS)[53–55] and EXAFS[28,55,56] were used. Notably, 2D ^{1}H-^{119}Sn D-HMQC MAS NMR spectroscopy has shown that the open and closed sites are dynamic, with their interconversion being primarily governed by temperature and hydration conditions. Specifically, at temperatures below 393 K, the zeolites favor the formation or preservation of open Sn sites, characterized by Sn–OH groups. Two types of open tin sites 6-coordinated and 4-coordinated associated with hydroxyl groups may coexist, which amount together to only 17% of all tin sites.[57] As the temperature increases to and above 393 K, these open Sn sites undergo dehydroxylation, transforming into closed Sn sites. Conversely, rehydration of the zeolite followed by dehydration at a moderate temperature around 393 K

can facilitate the reformation of open Sn sites from closed ones. Wolf et al.[31] have provided significant insights into the dynamic nature of Sn sites in Sn-Beta zeolites, focusing on how synthesis methods affect their catalytic properties. Employing Dynamic Nuclear Polarization (DNP) NMR and complementing it with DFT to calculate Chemical Shift Anisotropy (CSA) parameters, their research offered an in-depth perspective on the nature of sites in various synthesized Sn-Beta zeolites. After thermal treatment, the majority of these sites were observed to be 'closed', characterized by Sn(IV) centers tetrahedrally coordinated to the zeolite framework. Using ^{119}Sn NMR, they show that T6, T5, and T7 sites were predominant in hydrothermally synthesized Sn-Beta materials. Moreover, interaction with water could lead to partial hydrolysis of these closed sites, forming hydrolyzed-open sites, resulting in tri-coordinated Sn(IV) and the formation of Sn-OH bonds. Contrarily, Sn-Beta zeolites modified post-synthetically through a two-step method are likely to contain a mix of closed T8 and T5 hydrolyzed-open sites, along with T9 defect-open sites, within their hydrophilic, defective framework. This comprehensive analysis underscores the importance of zeolite morphology, like hydrophobicity or hydrophilicity, in determining their effectiveness, particularly in aqueous-phase isomerization of glucose.

Despite considerable advancements in understanding the properties of the M-Beta zeolites, significant gaps remain in our comprehensive understanding, particularly concerning the structure, stability, and behavior of closed and open sites for Sn and especially other metals within these zeolites. Unraveling the intricate geometric characteristics and Lewis acidity of these sites is crucial. This deeper insight is essential for establishing a clear link between these fundamental properties and their catalytic activity, thereby unlocking their full potential in a range of applications.

Here, we carry out an extensive periodic DFT investigation which is designed to illuminate the structure, stability, and Lewis acidity of both closed and open sites in these metal-substituted zeolites. We focus on the Beta zeolite family, a subject of considerable interest due to its high thermal stability and its ability to withstand strong acids, making it useful in

catalysis, particularly in the petrochemical.[58–61] We systematically examine various possible structures of open and closed sites in Sn-, Ti-, Zr- and Hf-substituted Beta zeolites at various T-site positions, and derive a first-principle thermodynamic model to determine the most stable structures in a set of operating conditions. Finally, we model the adsorption of pyridine as a probe molecule of Lewis acidity to compare the properties of the different sites.

2 Methods

2.1 Computational details

The computational investigations were carried out using the periodic Density Functional Theory (DFT) as implemented in the Vienna Ab initio Simulation Package (VASP) version 5.[62,63] In these calculations, the Projector Augmented-Wave (PAW) method was employed.[64,65] The number of valence electrons of the different atoms is reported in Table S1. The exchange-correlation functional was treated within the generalized gradient approximation (GGA) using the Perdew-Burke-Ernzerhof (PBE) functional,[66] with a D2 dispersion correction applied to account for van der Waals interactions.[67] The Brillouin zone sampling was performed at the Gamma point (Γ).

Beta zeolites usually exist as an intergrowth of three polymorphs. These include chiral polymorph A (see Fig. S1), achiral polymorph B, and polymorph C, as outlined in prior researches.[49,68–70] Historically, polymorph A has been extensively explored, but our research shifts attention to polymorph B. This choice is motivated by the common coexistence of polymorphs A and B within Beta zeolite, typically in a 60:40 ratio.[71] Polymorph B is particularly interesting because of its larger unit cell for the same number of atoms, which fully encompasses the complete pore system (see Fig. 2). This characteristic suggests that replicating the unit cell for simulation purposes may be unnecessary, potentially simplifying computational models and offering a more efficient pathway to understanding the zeolite's behavior. The initial unit cell parameters and atomic positions for polymorph B of Beta

zeolite with silicon were obtained from the International Zeolite Database.[72] To form M-Beta zeolites (M: Sn, Ti, Zr and Hf), one silicon atom was substituted with these metals, primarily at the T1, T6, and T9 sites, resulting in a unit cell comprising 128 oxygen atoms, 1 metal atom (Sn, Ti, Zr, or Hf), and 63 silicon atoms.

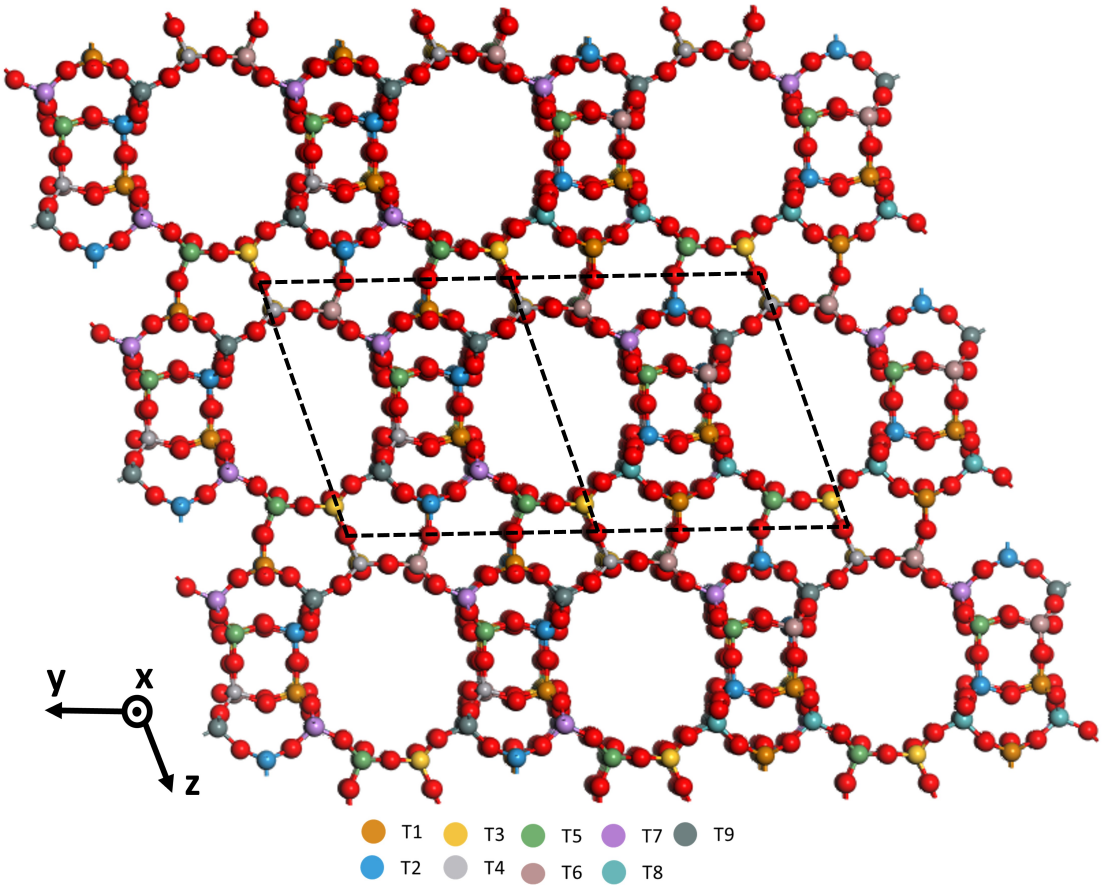

Figure 2: Three-dimensional framework of Zeolite Beta polymorph B illustrating the spatial arrangement of atoms within the crystalline matrix. The zeolite's porous architecture shows the distribution of different T sites. Each T site, labeled from T1 to T9, is color-coded for clarity as shown in the figure. The dashed lines delineate the unit cell boundaries within the crystal lattice. Atom color coding is consistent with common conventions where oxygen atoms are red and silicon atoms, which may occupy T sites similarly to silicon, are represented in their respective T site colors. The axes (x, y, z) are shown to provide a reference for the crystal orientation.

For the optimization of the M-substituted zeolites (hence structures featuring only closed sites), we employed a three-step geometry optimization procedure[73] to ensure the structural

stability and accurate representation of the zeolite structures. In the first step, one of the Si atom located on one of the T-sites from the Beta structure obtained from IZA was substituted by a M atom, and the positions of the atoms were relaxed without modification of the lattice parameters. For this step, we employed a plane-wave cutoff energy of 400 eV, and convergence criteria of 10^{-7} eV for the self-consistent field (SCF) cycle and of 0.02 eV Å^{-1} for the geometry optimization convergence. In the second step, both atom positions and cell parameters were allowed to relax with a higher plane-wave cutoff energy of 800 eV, with a geometry convergence criterion on the energy of the cell of 10^{-6} eV. We employed a higher cutoff in this step in order to limit the effects on the total energy caused by the variation of the cell volume, which induces a variation of the number of plan waves involved in the calculation. The unit cell parameters for the different T site and metal combinations after optimization are reported in Table S2. The analysis of unit cell parameters (a, b, c, α, β, and γ) across the different T-sites within zeolites display relatively minor variations (usually less than 0.5% relative across all combinations of T-site and metal, save for the case of the c axis for T6-Ti for which it is 1%). The final step consists in a geometry optimization at constant cell dimensions, starting from the output of the second step, with a 400 eV cutoff and a tighter geometry convergence criterion of 0.001 eV Å^{-1}. This last step constitutes the reference structure and energy at the chosen level of accuracy for a given site model. In the case of the adsorption of water and pyridine, we fixed the lattice parameters and employed the same calculation parameters as in the latter step. Subsequent to the final optimization, frequency calculations were performed to account for vibrational contributions to the Gibbs free energies. These calculations were conducted at a cutoff energy of 400 eV, following the finite difference approach to compute the Hessian matrix, with a displacement of ±0.01 Å on all atoms of the cell.

Charges were estimated thanks to the approach of Bader.[74,75] In the spirits of refs.,[76,77] the electrostatic field was calculated as the linearized gradient of the electrostatic potential (ionic plus Hartree plus exchange–correlation potential), itself calculated as implemented in

VASP, in the surrounding of the N atom of adsorbed pyridine (see later in the results part). To do so, we calculated the local electrostatic potential after removing the pyridine molecule, while keeping all other geometric features constrained. The gradient was computed between two points distant by 1 Å, in the Metal-N (from pyridine) axis, equidistant from the N position.

2.2 Reaction energies and free energies

This study comprehensively investigates the reaction energies to understand the stability and acidity of closed and open sites in zeolites, particularly in their interactions with water and pyridine molecules. We focus on two primary metrics: electronic energy differences ($\Delta_r E$) and free energy differences ($\Delta_r G$).

The initial step was calculating the electronic adsorption energy of water ($\Delta_r E_{\text{ads}}(H_2O)$) to assess the stability of closed sites and their transition to hydrated sites. The adsorption of water in both dissociated (as OH-H pairs) and non-dissociated (as H_2O) states was explored to determine the stability of various configurations.

In general, the electronic adsorption energy, denoted as $\Delta_r E_{\text{ads}}$, was computed using the formula:

$$\Delta_r E_{\text{ads}} = E_{\text{Zeo@mol}} - E_{\text{mol}} - E_{\text{Zeo}} \tag{1}$$

where $E_{\text{Zeo@mol}}$ is the electronic energy of the zeolite with the adsorbed molecule being water or pyridine, E_{mol} is the electronic energy of the molecule in the gas phase, and E_{Zeo} is the electronic energy of the bare zeolite. E_{mol} was determined from a separate calculation where the molecule is placed into a simulation box with dimensions of $40\,\text{Å} \times 40\,\text{Å} \times 40\,\text{Å}$.

After determining $\Delta_r E_{\text{ads}}$, we calculated the Gibbs free energy changes related to adsorption, denoted as $\Delta_r G_{\text{ads}}$(T,P). This includes detailed internal energy, enthalpy and entropy considerations. The standard Gibbs free energy change for adsorption, $\Delta_r G^{\circ}_{\text{ads}}(T)$, under

standard conditions (1 atm) includes these contributions:

$$\Delta_r G^\circ_{\text{ads}}(T) = \Delta_r E_{\text{ads}} + \Delta_r U^\circ_{\text{vib}} + \Delta_r H^\circ_{\text{rot+trans}} - T(\Delta_r S^\circ_{\text{vib}} + \Delta_r S^\circ_{\text{rot+trans}}) \tag{2}$$

In this formula, $\Delta_r E_{\text{ads}}$ represents the electronic adsorption energy, capturing the change in electronic energy as the molecule adsorbs onto the zeolite surface. Additionally, $\Delta_r U^\circ_{\text{vib}}$ accounts for the change in vibrational internal energy, $\Delta_r H^\circ_{\text{rot+trans}}$ represents changes in rotational and translational internal energy, T is the temperature in K and the entropy terms $\Delta_r S^\circ_{\text{vib}}$ and $\Delta_r S^\circ_{\text{rot+trans}}$ reflect alterations in vibrational, rotational, and translational entropy upon adsorption.

To evaluate the Gibbs free energy change at specific temperature (T) and pressure (P) environmental conditions, $\Delta_r G_{\text{ads}}(T, P)$, we utilized the following formula:

$$\Delta_r G_{\text{ads}}(T, P) = \Delta_r G^\circ_{\text{ads}}(T) + RT \ln\left(\frac{P}{P^\circ}\right) \tag{3}$$

For water adsorption, configurations up to the saturation point (defined as the maximal number of water molecules that can either adsorb on M by forming a new M-O bond, or hydrolyse a Si-O-M bond) were examined, considering sequential adsorption processes represented by n ranging from 1 to 6. The Gibbs free energy change for each adsorption step, $\Delta_r G_{\text{ads,n}}(T, P_{\text{H}_2\text{O}})$, was calculated as:

$$\Delta_r G_{\text{ads,n}}(T, P_{\text{H}_2\text{O}}) = G_{\text{Zeo@H}_2\text{O,n}}(T, P_{\text{H}_2\text{O}}) - n \cdot G_{\text{H}_2\text{O}}(T, P_{\text{H}_2\text{O}}) - G_{\text{Zeo}}(T, P_{\text{H}_2\text{O}}) \tag{4}$$

where $G_{\text{Zeo@H}_2\text{O,n}}(T, P_{\text{H}_2\text{O}})$ is the free energy of the zeolite with the adsorbed water at the n-th step of adsorption under conditions T and $P_{\text{H}_2\text{O}}$, $G_{\text{H}_2\text{O}}(T, P_{\text{H}_2\text{O}})$ is the free energy of the molecule in the gas phase under conditions T and $P_{\text{H}_2\text{O}}$, and $G_{\text{Zeo}}(T, P_{\text{H}_2\text{O}})$ is the free energy of the bare zeolite under conditions T and $P_{\text{H}_2\text{O}}$.

Predominance diagrams featuring two parameters (T, $P_{\mathrm{H_2O}}$) were then constructed using these results, where at each point the predominant species is that of lowest Gibbs free energy, thus the most stable. The temperature range considered spanned 290 to 1000 K, and the water pressure range varied from 10^{-6} to 1 bar.

The adsorption of pyridine was simulated on closed and open sites. One molecule was adsorbed to assess the Lewis acidity of the zeolite sites. The same methodology was applied to calculate the electronic adsorption energy ($\Delta_r E_{\mathrm{ads}}(Pyr)$) and free adsorption energy ($\Delta_r G_{\mathrm{ads}}(Pyr)(T, P_{\mathrm{Pyr}})$) of pyridine, enabling a comparative analysis across the Beta-M zeolites and the positions of the M atoms.

3 Results and discussions

3.1 Stability Analysis of T Sites in M-Beta Zeolites

We first aimed at identifying the most stable T site. We adhered to the T site numbering as defined by the International Zeolite Association. We carried out the complete investigation with M = Sn.

Specifically, we began with the introduction of Sn atoms into each of the nine distinct T positions of Sn-Beta, maintaining a Si/Sn ratio of 63. The stability of these sites is reported in Fig. S2, showing T7 as the most energetically favorable position and T8 as the least stable. The figure also shows a closely balanced stability profile across the T sites as the difference between the most and least stable stable is lower than 15 kJ mol^{-1}. On the basis of this small energetic span between the positions, most sites may thus be considered as having similar probabilities of existence which is in agreement with previous theoretical studies.[31,32,43]

In our study focusing on Beta zeolite polymorph B, we strategically selected T1, T6, and T9 sites based on insights derived from the seminal work of Kolyagin et al.[30] Their observations allowed for categorizing the tin sites in Sn-Beta materials containing a mixture of A and B polymorphs, into three distinct groups based on their chemical properties. Group

I (assigned to T3, T4, T9 with respect to nomenclature in polymorph A) known for high Lewis acidity and hydrolyzing ability; Group II (T1, T2, T8 in polymorph A) with low Lewis acidity but very high hydrolyzing potential; and Group III (T5-T7 in polymorph A), which are less reactive due to their energetically favorable positions.

In our study, we aimed to choose one representative T site from each group to ensure a comprehensive analysis. To translate these findings to polymorph B, we established correspondence between the T sites of polymorphs A and B, as detailed in Table S3. Accordingly, we selected T1 in polymorph B as representative of Group II (corresponding to T2 in A), T6 for Group I (corresponding to T3 in A), and T9 for Group III (corresponding to T7 in A). This selection allows us to explore a range of catalytic behaviors and reactivities in the context of polymorph B, enriching our understanding of zeolite properties beyond the commonly studied polymorph A.

3.2 Water adsorption on metal sites

We then examine the hydration of closed sites. In our approach, we drew inspiration from the methodology originally proposed by Josephson et al.[43] for the adsorption of a single molecule on Sn, with the added incorporation of non-dissociated water molecules and the inclusion of metals beyond Sn, such as Ti, Zr, and Hf. We carefully examined the water adsorption process up to the saturation point with 6 water molecules after which no Si-O-M bond is left to hydrolyze, vide infra. This comprehensive study allowed us to map out a large set of open site configurations, both stable and unstable.

As shown in Fig. 3, our results for the T1-Sn sites show that the adsorption of molecular, non dissociated water molecule is the most exothermic adsorption mode that we obtained ($\Delta_r E_{\text{ads}}(\text{H}_2\text{O}) = -65$ kJ mol^{-1}). This is consistent with the findings of Bukowski et al.[44] Their study showed that non-dissociated water adsorption mode on the closed site is energetically favorable, and dissociation on an adjacent oxygen site requires an activation free energy barrier of 0.75 eV. This suggests a strong interaction between the water molecule

and the tin site, comparable to the interaction strength between water and aluminum in aluminosilicate zeolites.[78] The dissociative adsorption modes, either in Syn configuration where both hydroxyl groups are located on the same half-space with respect to the Sn atom ($\Delta_r E_{\text{ads}}(\text{H}_2\text{O}) = -41$ kJ mol^{-1}) or in Anti configuration (both hydroxyl groups in opposite half-spaces with respect to the Sn atom, characterized by the Si-O-Sn-OH arrangement, with $\Delta_r E_{\text{ads}}(\text{H}_2\text{O}) = -46$ kJ mol^{-1} are significantly less stable. The fact that the Anti configuration is more stable than the Syn configuration is in line with previous results from the literature.[43,46,57,79]

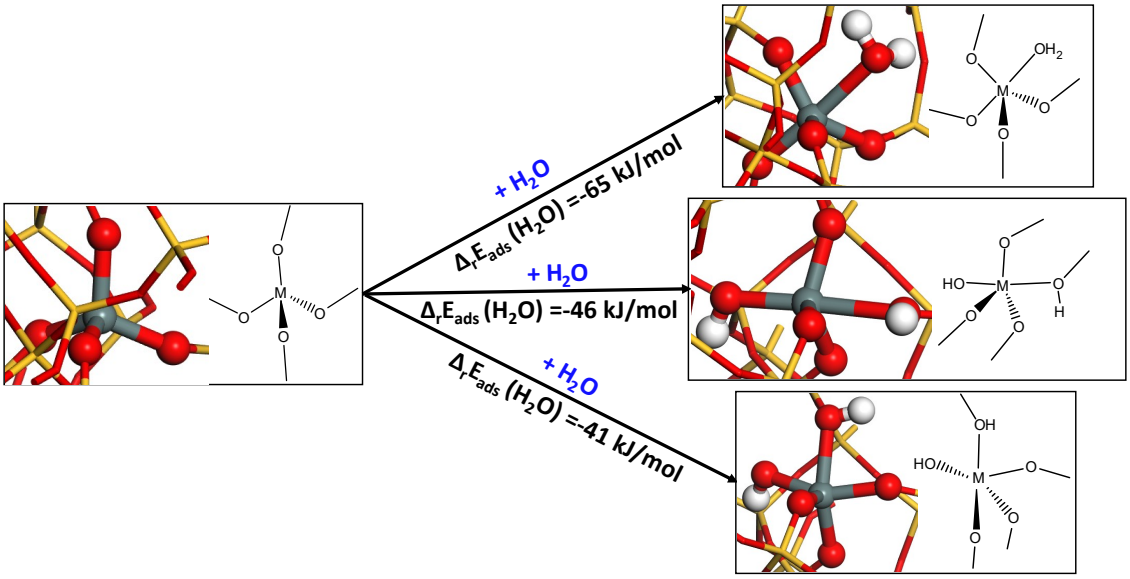

Figure 3: Most relevant adsorption modalities of a single water molecule on T1 site with Sn metal demonstrated through molecular simulations. The first path represents the non-dissociated adsorption form of water. The second path shows the dissociated state with the protonated Sn-O-Si bridge positioned diametrically opposite to the SnOH group, indicating a Anti configuration. The third path illustrates the Syn adsorption mode, where both the protonated Sn-O-Si bridge and the SnOH group are on the same side. In the specific dissociated adsorption configurations shown, Si-O-Sn hydrolysis does not take place, the Si-O-M bridge being simply protonated, and the bridge maintained. The atom color coding is as follows: hydrogen (H) is white, oxygen (O) is red, silicon (Si) is yellow, and tin (Sn) is dark grey.

This result is qualitatively very general, as we reach similar conclusions for each T-site (T1, T6 and T9) and each metal (Sn, Ti, Zr, Hf) under investigation (see Table S4). We thus observed a clear energetic preference for the adsorption of non-dissociated water molecules

across all metals.

Most of the time, the dissociative adsorption mode does not form a truly open site, as the hydration does not lead to the full hydrolysis of a M-O-Si bridge: instead of being broken, the bridge is simply protonated and the M hydration extends its coordination to five. Indeed, in the Anti configuration, the metal atoms adopt a pentacoordinated pseudo bipyramidal geometry, with one M-OH bond significantly longer than the other (typically, 2.36 Å vs. 1.99 Å for Sn at T1).

We extended our study with an advanced understanding of metal site full hydration by analyzing the adsorption of up to six water molecules, a scenario not explored in previous research. For each level of hydration, we analyzed various orientations and adsorption modes (dissociative or not), identifying the most stable configuration at each step. Table S5 presents the adsorption energies for the most stable configuration at each hydration level, representing a selective subset of calculations from a total of around 1944 computations. The data illustrates a trend where the adsorption energies become increasingly negative, as the number of water molecules adsorbed rises. This trend is consistent across all three T sites and is observed for all considered metals, with the exception of Ti at T6. A comparative analysis of the metals shows that water adsorbs with significantly higher affinity on Hf and Zr, in contrast to Sn and Ti. The dispersion component values of $\Delta_r E_{\text{ads}}$, as shown in Table S5, do not explain the differences in hydrophilicity observed among the sites and metals. To probe further into this phenomenon, we conducted a Bader charge analysis,[80–83] examining the partial charge distributions of the metals and adjacent oxygen atoms, seeking explanations for the observed adsorption behaviors. This analysis is visually represented in Fig. S3, with charges quantified in atomic charge units. For Sn, a partial charge of +2.4 is observed, with the nearby oxygen atoms carrying a charge of -1.4. In the case of Ti, the metal exhibits a partial charge of +2.2, and the associated oxygen atoms have a charge of -1.3, suggesting a marginally weaker ionic bond in comparison to Sn. Conversely, Zr and Hf show evidence of stronger ionic bonding, with partial charges of +2.6 and +2.5, respectively, and

an oxygen charge of -1.4, pointing to a nuanced interplay between metal type and adsorption characteristics.

Fig. 4 shows the different geometries obtained along hydration progression of the T1 site for all the metals. In the center of the figure, the non-hydrated state (a), the metal is in a four-coordinate environment, bound to oxygen atoms in the zeolite framework.

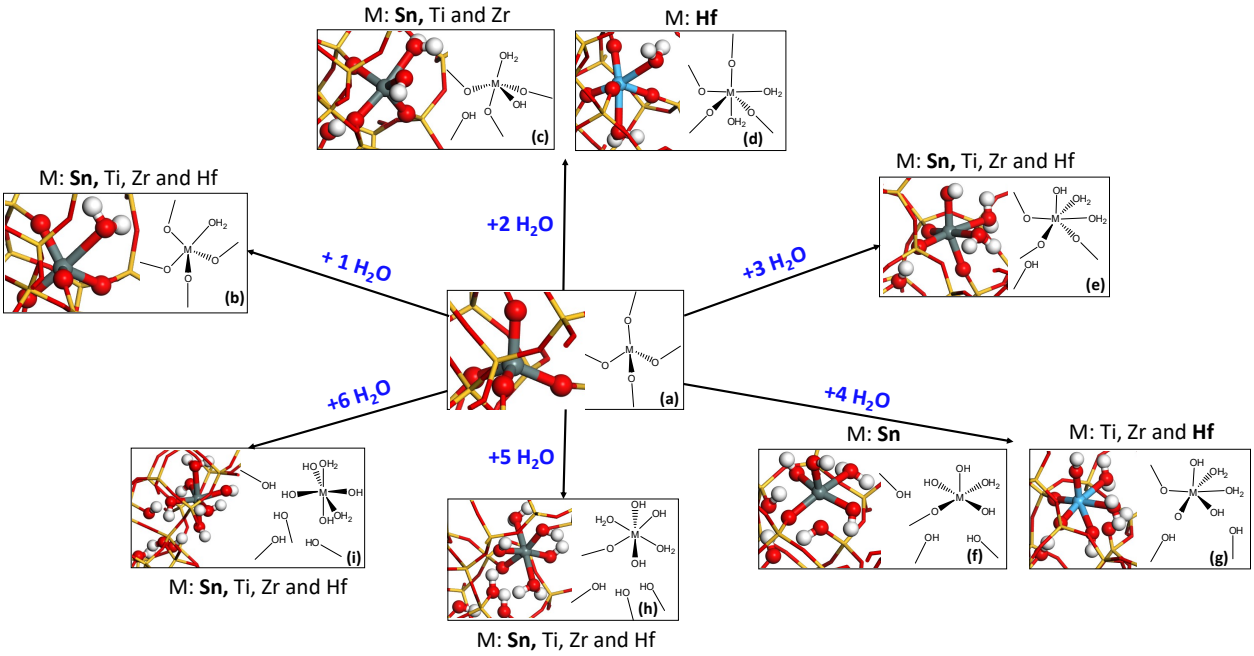

Figure 4: Most favorable structures determined for the progressive coordination of water molecules (0 to 6) at the T1 site for different metals (M), specifically Sn, Ti, Zr, and Hf. The metal displayed in each image is indicated in bold. The central image (a) represents the initial, dehydrated state of the site. Moving outward from the center, each panel (b) to (i) shows the site with an increasing number of water molecules bonded. The atom color coding is as follows: hydrogen (H) is depicted in white, oxygen (O) in red, silicon (Si) in yellow, and the metals (M) are shown in either dark grey or blue sky for distinction.

With the introduction of the first water molecule (b), as mentioned above, all metals exhibit a preference for the adsorption of non-dissociated water. As we progress to the adsorption of two water molecules, a divergence appears; Sn, Ti, and Zr (c) favor one non-dissociated water molecule while the second in a dissociative adsorption mode forming a Anti configuration. In this case, a Si-O-M bridge is hydrolyzed, with M-O bond breaking, so that we can qualify the M as an hydrated open site, exhibiting a five-fold coordination. Hf (d), however, maintains both water molecules in a non-dissociative mode, thus lying in a six-fold

coordinated state. Introducing a third water molecule (e) unveils a consistent pattern across all metals, with two non-dissociative and one dissociative Anti configuration, suggesting a shift towards more complex hydration as the T1 site becomes more saturated. The metal atom lies in octahedral coordination, explaining that further hydration involves more M-O-Si bridges hydrolysis. With four water molecules, Sn (f) displays a unique behavior with one non-dissociative and three dissociative Anti-configured water molecules, whereas the other metals (Ti, Zr, Hf) (g) show two molecules in non-dissociative adsorption mode and final water molecule in dissociative Anti-configured mode. With five water molecules, the system reaches a uniform state across all metals (h), two non-dissociative and three dissociative. Upon the coordination of six water molecules, each metal—Sn, Ti, Zr, and Hf (i) undergoes a significant transformation from its initial four-coordinate state bound to oxygen atoms within the zeolite framework. This stage represents a critical shift where the metals detach from the zeolitic framework. This detachment is a crucial observation as it signifies the saturation point beyond which the metal can no longer maintain its position within the zeolite structure. While this outcome does not come as a surprise considering the steric and electronic repulsions introduced by multiple water molecules, it has significant implications for the application of these metal-doped zeolites in catalysis. The detachment of the metal centers at high hydration levels exposes a limitation in the stability of Lewis acidic sites in aqueous environments. The findings reported herein for the T1 site are generally transposable to sites T6 and T9, with only slight variations that do not alter the main conclusions.

Our findings highlight the dynamic nature of metal coordination in zeolites under hydration. The detachment of metals at a six-water molecule state emphasizes the need for a careful balance in metal doping for Lewis acidity and hydration management.

In light of the preliminary findings, our investigation progressed beyond the initial assessment of electronic energy changes ($\Delta_r E_{\text{ads}}(\text{H}_2\text{O})$) and we advanced our analysis to the evaluation of Gibbs free energy ($\Delta_r G_{\text{ads}}(\text{H}_2\text{O})(T, P_{\text{H}_2\text{O}})$), employing first-principles thermodynamics as previously described. In this context, we construct phase diagrams (Fig. 5),

color-coded to indicate the number of interacting water molecules, to specifically illustrate the differential stability of these sites. The diagrams represent the most stable structure for each condition (T, P_{H_2O}).

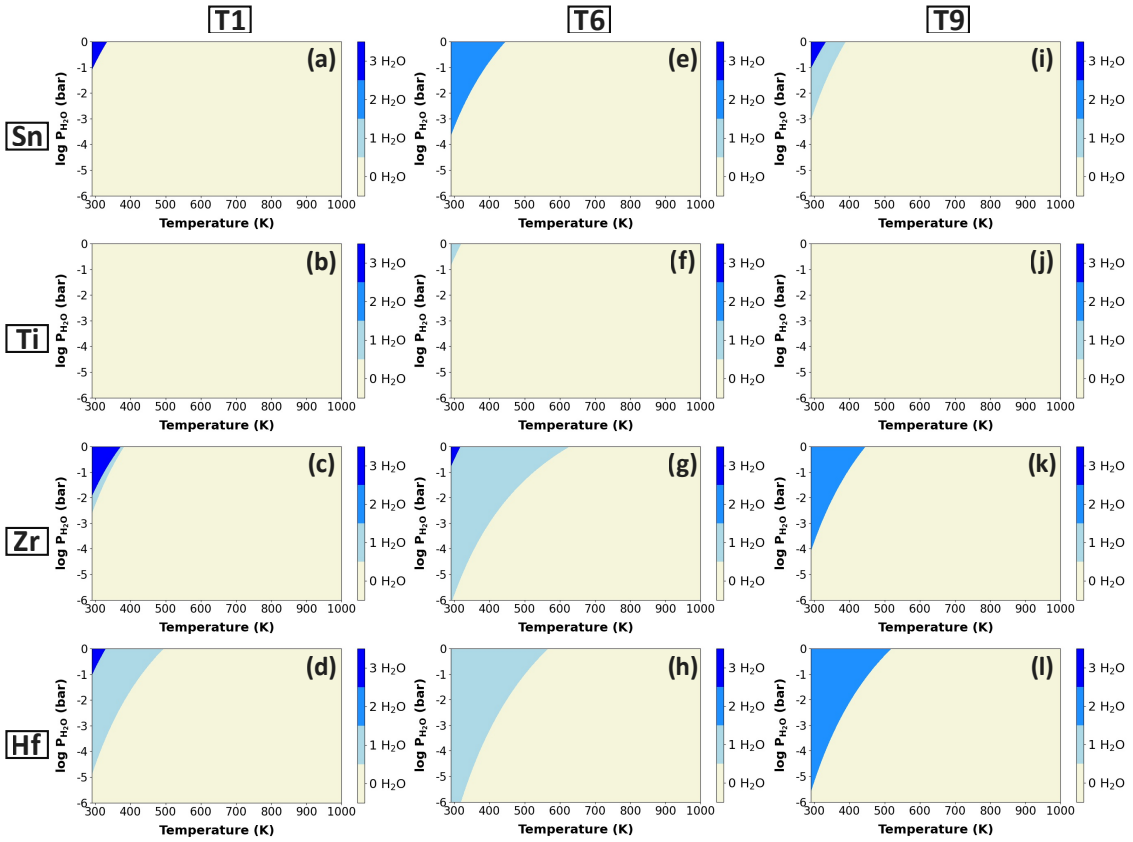

Figure 5: Different phase diagrams for T1, T6, and T9 sites within a zeolite framework, comparing the stability of non-hydrated and hydrated states under a range of temperatures (K) and water pressures (bar). Each row represents a different metal dopant (Sn, Ti, Zr, and Hf), and each column corresponds to one of the T sites. The diagrams illustrate the transition between hydration levels from 0 to 3 water molecules (H_2O) as denoted by the color gradient, where deeper shades indicate a higher number of coordinated water molecules. Models with a number of water molecules adsorbed higher than 3 are included in the model, but since they are not predominant in any case in the (T,P) range considered, we omitted the corresponding colour code for these hydration levels.

Considering the T1 site and Sn metal combination (T1-Sn) as an example, we show in Fig. 5-a that closed, non-hydrated configuration prevails across a wide temperature range from 300 K to 1000 K at low water pressures. A transition to a hydrated state occurs at ambient temperature and water pressures exceeding 10^{-1} bar, where T1-Sn site can interact

with three water molecules to form an open site with two non dissociated water molecules and one dissociated water with Anti configuration (see Fig. 4-e).

We then compared the effect of varying the nature of the metal in a given T site, with the example of T1. In the case of T1-Zr (Fig. 5-c), qualitatively the same hydration states exist on the diagram, though their stability domains are larger than the case of T1-Sn. T1-Hf (Fig. 5-d) site accommodates a single non-dissociated water molecule at temperatures below 500 K with water pressures approaching 10^{-1} bar, yet retains its closed structure. Converging with T1-Sn and T1-Zr, the T1-Hf site requires ambient temperatures and water pressures exceeding 10^{-1} bar to adopt an open configuration, where it then hosts two non-dissociated and one dissociated water molecule. T1-Ti (Fig. 5-b) site presents a unique case; Ti maintains a closed configuration with no interacting water molecules throughout the entire temperature and water pressure range examined. This indicates a remarkable stability and resistance to hydration, which could be particularly advantageous for low-temperature applications where water is a byproduct rather than a reactant.

Next, we compared the T sites for the same metal, Sn. T6-Sn (Fig. 5-e) shows different hydration behavior compared to T1-Sn. Its phase diagram displays a smaller temperature range with a stable closed site with 0 water molecule. Around 500 K and moderate pressures, the closed hydrated site configuration that accommodates two non-dissociated water molecules becomes favored. This distinct feature of T6-Sn sites suggests they have the capacity to interact with water molecules while maintaining their closed configuration.

T9-Sn site (Fig. 5-i) exhibits a predominance domain of closed, dehydrated site for temperatures above approximately 400 K. As the temperature decreases and pressure increases, the predominance domain of the closed site with one non-dissociated water molecule emerges, while at the lowest temperatures and highest pressures studied, a transition to an open site configuration accommodating three water molecules occurs, similar to T1-Sn.

This comprehensive analysis overall depicts a complex interplay between the dopant metal, position of the T site, temperature, water pressure, and hydration behavior. T1-Hf

and T1-Zr sites are more prone to hydration under specific conditions, likely due to the particular characteristics of Hf and Zr metals that facilitate water adsorption and dissociation. The moderate hydration interaction observed with T1-Sn suggests potential for a controlled hydrolytic process, which may be advantageous in certain catalytic reactions.

3.3 Probing acidity with pyridine

In this last part of our discussion, we try to answer a question which is central in our study: how does the Lewis acidity vary accross T-sites and metals, and how hydration affects the acidity of each metal in the different T sites ? We investigated the adsorption of pyridine, a typical probe molecule for acid site characterization,[84,85] under a pyridine pressure (P_{Pyr}) of 10^{-4} bar and a temperature of 298.15 K, which are representative conditions of adsorption of pyridine experiments.[86–89] We modelled the adsorption of pyridine on the non-hydrated sites and the hydrated-sites with non-dissociated H_2O and the Anti dissociated H_2O. As shown in Table S6, all the adsorption Gibbs free energies of the pyridine for all the studied sites and metals are negative, indicating that the adsorption process is thermodynamically favorable and spontaneous under a pyridine pressure of 10^{-4} bar and a temperature of 298.15 K.

Fig. 6 shows the molecular structures for the different modes of pyridine adsorption on the non-hydrated and hydrated T1 site for all the metals that we consider.

We begin with the depiction of the T1 site in its non-hydrated form (a) in Fig. 6i. In this state, the metal atoms (Sn, Ti, Zr, and Hf) are primed for direct coordination with the nitrogen atom of pyridine. The resulting interaction, demonstrated in (b), confirms the Lewis acidic nature of the T1 site in its dehydrated form, a characteristic consistently observed across the T6 and T9 sites under similar conditions.

Transitioning to the hydrated scenarios in Fig. 6ii, we first observe the T1 site coordinated with a non-dissociated water molecule (c), followed by the outcomes of pyridine adsorption (d and e). For metals such as Sn, Zr, and Hf (d), the nitrogen atom of pyridine interacts with the hydrogen atom of the water molecule, and a proton transfer to the pyridine occurs

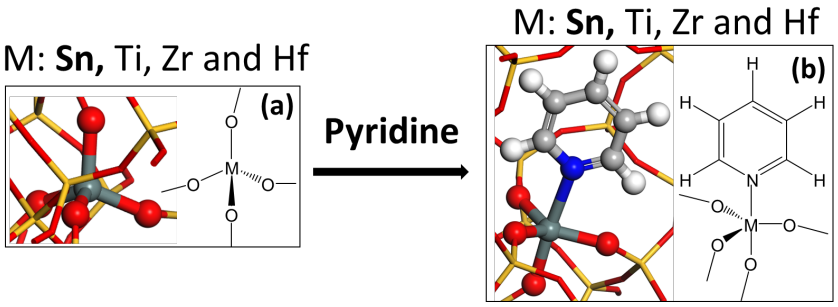

(i) Non-hydrated T1 site

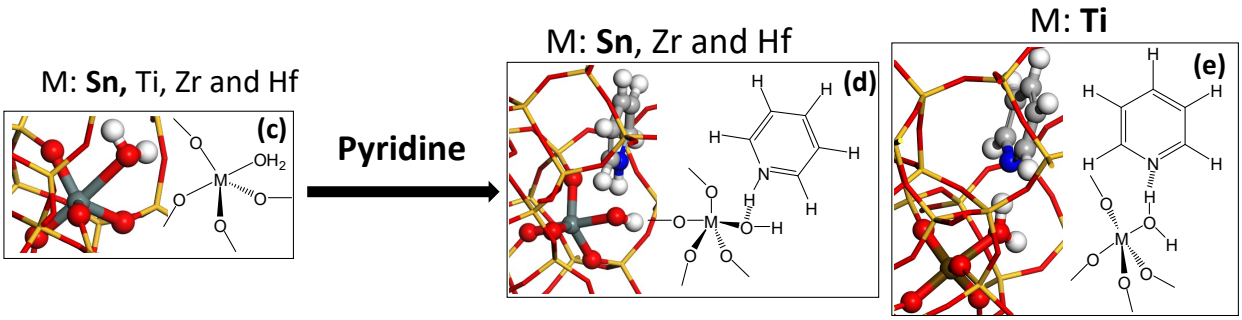

(ii) T1 site with a non-dissociated water molecule

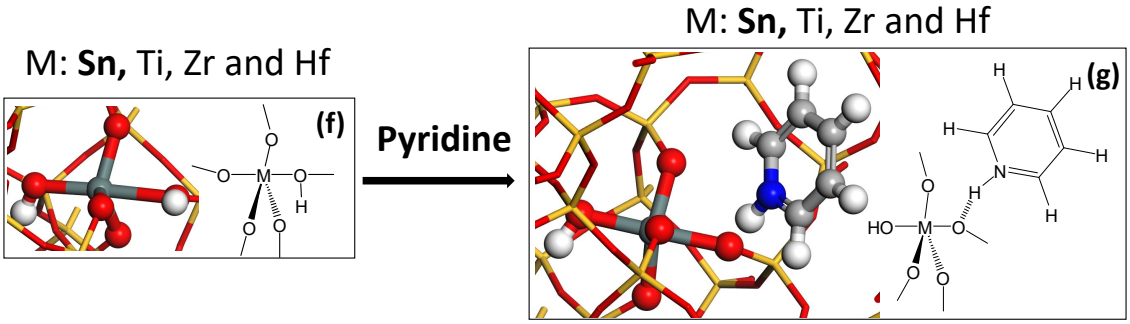

(iii) T1 site with a Anti dissociated water molecule

Figure 6: Adsorption of pyridine on T1 sites: (i) non-hydrated closed T1 site, (ii) the closed T1 site with a coordinated non-dissociated water molecule, and (iii) the T1 site with a dissociated water molecule. The visualizations detail pyridine interaction at the T1 sites across metal dopants (Sn, Ti, Zr, and Hf), emphasizing the variations in molecular orientation and bonding configuration resulting from the presence and state of water. The atom color coding is as follows: hydrogen (H) in white, carbon (C) in silver, nitrogen (N) in blue, oxygen (O) in red, silicon (Si) in yellow, and the metals (M) in either dark grey or brown for distinction.

wih the formation of a pyridinium, which typifies Brønsted acidity. In the case of titanium (e), the interaction is characterized by hydrogen bonding without proton transfer. Other modes of adsorption, including the formation of a Lewis acid-base pair through the direct coordination of pyridine with the metal (thus, to the co-adsorption of water and pyridine on the same metallic center), are not feasible for Sn and Ti (spontaneous desorption was observed). In the cases of Zr and Hf, although this process can be optimized, it leads to significantly reduced stability compared to the Brønsted adsorption mode, as illustrated in Fig. S4ii. In Fig. 6iii, we explore the T1 site with a dissociated water molecule (f), followed by the resultant state after pyridine adsorption (g). In that case, the most favorable mode of adsorption for all metals consists in the formation of a pyridinium ion after transfer of the proton from the Si−OH−M hydroxyl group. Adsorption mode such as Lewis acid-base pairs appears to be less stable (see Fig. S4iii). Thus, hydrated sites, if present, should manifest upon pyridine adsorption primarily as Brønsted acid sites. Note that the hydrated site may still express Lewis acidity provided that the water molecule is displaced by the pyridine molecule. This exchange has typically a standard reaction free energy of -78 kJ mol^{-1} at 298.15 K in the case of T1-Sn (the other values for the other sites are reported in Table S7), which means that it is favorable when partial pressures of water and pyridine are the same. In practice however, the thermodynamic feasibility of such a reaction will depend on the respective chemical potentials (partial pressures) of pyridine and water.

From Fig. 6i through 6iii, our findings underscore the dynamic interplay between hydration states and acid properties within Beta zeolite. While the non-hydrated sites (a) demonstrate the strongest Lewis acidity, the hydrated sites (c and f) primarily exhibit Brønsted acidity. This multifaceted nature of the T sites, influenced by water association and dissociation, shows the complex versatility of M-Beta zeolite catalytic sites.

In order to quantitatively compare the Lewis acidity of the various sites, we calculated the desorption temperature of pyridine as the temperature at which $\Delta_r G_{\text{ads}}(\text{Pyr})(T, P_{\text{Pyr}})$ becomes positive (see Fig. S5). We considered here only the adsorption on the closed sites

according to the adsorption mode depicted on Fig. 6i, as this is the most probable state of the sites after usual preparation conditions before experimental measurements (around 723 K and 10^{-6} bar),[86–89] see Fig. 5. A stronger Lewis acidity of the site is traduced by a higher desorption temperature. Our comparative analysis extends to a variety of metals (Sn, Ti, Zr, and Hf) and focuses on their Lewis acidity at the T1, T6, and T9 sites, as summarized in Table 1.

Table 1: Desorption temperatures (K) of pyridine across different metals and sites.

Metal/Site	T1	T6	T9
Sn	537	631	470
Ti	370	411	353
Zr	551	581	462
Hf	552	606	546

Two key observations emerge from the table analysis. Firstly, Ti consistently exhibits the lowest desorption temperature across all metal and T-site combinations, indicating its relatively lower Lewis acidity. Secondly, while the Lewis acidity ranking of the other metals varies depending on the T-site, a consistent pattern emerges within each metal: the desorption temperatures are invariably lower at the T9 site, suggesting reduced acidity of metal species at this position. Conversely, the T6 site appears to foster the strongest Lewis acid sites, with T1 representing an intermediate scenario. Notably, across all evaluated systems, T6-Sn demonstrates the highest Lewis acidity, whereas T9-Ti shows the lowest. This observation is in line with previous experimental research, which found that the density and strength of Lewis acidity induced by metal ion incorporation follow the sequence: Sn-Beta > Zr-Beta > Ti-Beta.[90] Supporting these findings, Kulkarni et al.[91] conducted a theoretical study on the Lewis acidity and reactivity of Sn- and Ti-substituted Beta zeolites. Their conclusion, that Sn-Beta exhibits greater Lewis acidity compared to Ti-Beta, corroborates our results.

To attempt to explain these differences, we carried out a series of additional analysis that delve into different factors possibly linked to the Lewis acidity between the metals and the

T sites investigated.

Firstly, we decomposed the adsorption energy into its various components, including electronic interaction, deformation of each member (zeolite and pyridine) upon adsorption, and dispersion energy as indicated in the schematic in Fig. S6i. The quantitative measures of these components are presented in Fig. S6ii. The examination of this decomposition shows that the main driver is the difference in the electronic interaction energy term, for which a good correspondence with the desorption temperature is found (see Fig. S7i), though this needs to be nuanced. Sn sites have stronger electronic interaction with pyridine ($\Delta_r E_{\mathrm{DFT}} = -140$ to -160 kJ mol^{-1}, versus -130 to -100 kJ mol^{-1} for Zr and Hf, and -100 to -80 kJ mol^{-1} for Ti), however, the deformation of the site caused by adsorption is more detrimental ($\Delta_r E_{\mathrm{def}}$(Zeo) = 60-80 kJ mol^{-1} compared to 30-50 kJ mol^{-1} for the other metals) which somehow negates the effect of the stronger electronic interaction (see Fig. S7ii). The dispersion contribution ranges from $\Delta_r E_{\mathrm{dispersion}} = -60$ to -80 kJ mol^{-1} for all species and is not discriminant (see Fig. S7iii).

Fig. S3 illustrates the variations in partial charge distributions for metals at different T sites, as determined through Bader charge analysis.[80–83] Ti consistently feature a slightly lower positive charge compared to the other metals, which have among them the same charge distribution. No difference is observed between the T sites. This overall suggests that charge distribution alone does not significantly affect the variations in Lewis acidity.

Finally, we calculated the local electrostatic field at the adsorption site. Fig. S7iv shows the relationship between electrostatic field strength at the adsorption sites and the corresponding desorption temperatures of pyridine. We find that larger electrostatic fields tend to correspond to higher desorption temperatures of pyridine, with for instance Ti having the lowest local field than the other metals, and in the cases of Zr and Sn desorption temperature increases almost linearly with the electrostatic field across the different T-sites. However, the relationship is not systematically followed and is mostly qualitative, which we may interpret as a significant contribution though other factors may interfere, as discussed above.

Our results show that the hydration and Lewis acid properties of a given metal are significantly affected by the position in the network. This is qualitatively consistent with the observations made by Kolyagin et al.[30] on Sn-Beta zeolites, and we may compare our results with their experimental findings. In their contribution, they distinguished three groups of sites, labelled Group I, II and III, characterized by their position in the lattice, tendency to hydrolyze and catalytic activity, which may be related to Lewis acidity. As described above, they are represented in our study respectively by T6, T1 and T9. Group II is the most prone to being hydrolyzed, and shows the highest acidity, on par with that of Group I, while Group III shows both low hydrolysis ability and low activity. The results regarding the Lewis acidity is very consistent with these experimental results, as we found a significantly lower Lewis acidity for T9-Sn than for the other sites, though we do observe a difference between T1-Sn and T6-Sn. Regarding the hydrolysis ability, we find roughly similar domains of stability of hydrolyzed sites for T6-Sn and T9-Sn, but T1-Sn has the smallest domain comparatively (see Fig. 5). This is not consistent with the observations, however, note that our analysis represents only thermodynamics, while kinetic considerations that we did not model might be at stake in the process. This might also be related to the differences in polymorphs of the Beta zeolites (B in our study, while a mixture is employed by Kolyagin et al., which might affect the correspondence). Last but not least, we also did not consider the external surface sites, which may also contribute to the experimental behaviors observed. We further extend the scope beyond Sn and show that this may be generalized to Titanium (Ti), Zirconium (Zr), and Hafnium (Hf) exchanged zeolites.

4 Conclusions

We employed periodic DFT calculations to investigate the stability and structural properties of closed, hydrated and open T sites in zeolite Beta doped with Sn, Ti, Zr and Hf. A notable conclusion of the study is the preferential adsorption of non-dissociated water

molecules on all metals, challenging traditional expectations of tetrahedral open sites. By applying first-principles thermodynamics, we have generated diagrams covering a wide range of temperature (T) and pressure (P) conditions, describing the most stable configurations in terms of water coverage, coordination state of the metal, and water adsorption mode (non-dissociative, dissociative, with or without M-O-Si bridge hydrolysis). Our results show that regardless of the type of metal and its specific T-site position within the zeolite framework, closed site configurations are predominantly favored under a wide range of conditions. The degree of hydration and the preferred structural configurations are dependent on both the type of metal dopant and its specific T-site position, emphasizing the intricate interplay between the metal properties and the zeolite structure. Adsorption of pyridine, a well-established probe for characterization of Lewis and Brønsted acid sites, exposes nuanced differences in Lewis acidity between the different closed T sites and metal dopants. T6 sites with Sn proved to be particularly strong Lewis acids, while T9 sites with Ti showed the lowest pyridine desorption temperatures. Energy decomposition, Bader charge analyses and electrostatic field estimations were conducted to conclude about the most influential parameters playing on the Lewis acidity. In the case of hydrated sites, according to pyridine adsorption, adsorbed water molecules and M-(OH)-Si groups are expected to behave as Brønsted acid sites. This thermodynamic perspective provides a solid foundation for future research and, in particular, points to the need for kinetic studies to complement our findings, in particular regarding the hydrolysis ability of given T sites. It also put the basis for next works to establish structure-acidity-activity relationships in a variety of catalytic reactions.

Acknowledgement

This research was partly funded by the French Agence Nationale pour la Recherche (ANR) in the frame of the SELECTOSZE project ANR-21-CE07-0043-01. Calculations were performed using HPC resources from GENCI-CINES (Grant A0140806134) and from IFP En-

ergies nouvelles (ENER440).

Supporting Information Available

Additional Figures and Tables (PDF). The coordinates of all periodic systems reported herein are added as a .zip archive (ZIP).

Conflict of Interest

No conflict of interest to declare.

Author information

4.1 Corresponding author

Kim Larmier - IFP Energies nouvelles, Rond-Point de l'Echangeur de Solaize, BP3, 63960, Solaize, France; orcid.org/0000-0002-5199-1516; Email: kim.larmier@ifpen.fr

4.2 Authors

Nawras Abidi - IFP Energies nouvelles, Rond-Point de l'Echangeur de Solaize, BP3, 63960, Solaize, France; orcid.org/0000-0002-4600-0044

Yacine Boudjema - IFP Energies nouvelles, Rond-Point de l'Echangeur de Solaize, BP3, 63960, Solaize, France

Céline Chizallet - IFP Energies nouvelles, Rond-Point de l'Echangeur de Solaize, BP3, 63960, Solaize, France; orcid.org/0000-0001-5140-8397

References

(1) Colella, C.; Gualtieri, A. F. Cronstedt's zeolite. *Microporous Mesoporous Mater.* **2007**, *105*, 213–221.

(2) Dyer, A. *An Introduction to Zeolite Molecular Sieves*; John Wiley and Sons Inc., New York, NY, 1988.

(3) Corma, A. From Microporous to Mesoporous Molecular Sieve Materials and Their Use in Catalysis. *Chem. Rev.* **1997**, *97*, 2373–2420.

(4) Pérez-Botella, E.; Valencia, S.; Rey, F. Zeolites in Adsorption Processes: State of the Art and Future Prospects. *Chem. Rev.* **2022**, *122*, 17647–17695.

(5) Ham, K.; Kim, B. S.; Choi, K.-Y. Enhanced ammonium removal efficiency by ion exchange process of synthetic zeolite After Na^+ and heat pretreatment. *Water Sci. Technol.* **2018**, *78*, 1417–1425.

(6) Zhang, Q.; Gao, S.; Yu, J. Metal Sites in Zeolites: Synthesis, Characterization, and Catalysis. *Chem. Rev.* **2022**, *123*, 6039–6106.

(7) Chizallet, C.; Bouchy, C.; Larmier, K.; Pirngruber, G. Molecular Views on Mechanisms of Brønsted Acid-Catalyzed Reactions in Zeolites. *Chem. Rev.* **2023**, *123*, 6107–6196.

(8) Ennaert, T.; Van Aelst, J.; Dijkmans, J.; De Clercq, R.; Schutyser, W.; Dusselier, M.; Verboekend, D.; Sels, B. F. Potential and challenges of zeolite chemistry in the catalytic conversion of biomass. *Chem. Soc. Rev.* **2016**, *45*, 584–611.

(9) Moliner, M. State of the art of Lewis acid-containing zeolites: lessons from fine chemistry to new biomass transformation processes. *Dalton Trans.* **2014**, *43*, 4197–4208.

(10) Suib, S. L.; Přech, J.; Szaniawska, E.; Čejka, J. Recent Advances in Tetra-(Ti, Sn, Zr, Hf) and Pentavalent (Nb, V, Ta) Metal-Substituted Molecular Sieve Catalysis. *Chem. Rev.* **2022**, *123*, 877–917.

(11) Dartt, C.; Davis, M. Applications of zeolites to fine chemicals synthesis. *Catal. Today* **1994**, *19*, 151–186.

(12) Ma, Z.; Zaera, F. Heterogeneous Catalysis by Metals. *Encyclopedia Inorg. Chem.* **2006**,

(13) Pimentel, B. R.; Parulkar, A.; Zhou, E.-k.; Brunelli, N. A.; Lively, R. P. Zeolitic Imidazolate Frameworks: Next-Generation Materials for Energy-Efficient Gas Separations. *ChemSusChem* **2014**, *7*, 3202–3240.

(14) Vermeiren, W.; Gilson, J.-P. Impact of Zeolites on the Petroleum and Petrochemical Industry. *Top. Catal.* **2009**, *52*, 1131–1161.

(15) Mazur, M.; Kasneryk, V.; Přech, J.; Brivio, F.; Ochoa-Hernández, C.; Mayoral, A.; Kubů, M.; Čejka, J. Zeolite framework functionalisation by tuneable incorporation of various metals into the IPC-2 zeolite. *Inorg. Chem. Front.* **2018**, *5*, 2746–2755.

(16) Rodríguez-Fernández, A.; Di Iorio, J. R.; Paris, C.; Boronat, M.; Corma, A.; Román-Leshkov, Y.; Moliner, M. Selective active site placement in Lewis Acid zeolites and implications for catalysis of oxygenated compounds. *Chem. Sci.* **2020**, *11*, 10225–10235.

(17) Zhang, H.; bin Samsudin, I.; Jaenicke, S.; Chuah, G.-K. Zeolites in catalysis: sustainable synthesis and its impact on properties and applications. *Catal. Sci. Technol.* **2022**, *12*, 6024–6039.

(18) Bermejo-Deval, R.; Orazov, M.; Gounder, R.; Hwang, S.-J.; Davis, M. E. Active Sites in Sn-Beta for Glucose Isomerization to Fructose and Epimerization to Mannose. *ACS Catal.* **2014**, *4*, 2288–2297.

(19) Corma, A.; Nemeth, L. T.; Renz, M.; Valencia, S. Sn-zeolite beta as a heterogeneous chemoselective catalyst for Baeyer-Villiger oxidations. *Nature* **2001**, *412*, 423–425.

(20) Corma, A.; Domine, M. E.; Nemeth, L.; Valencia, S. Al-Free Sn-Beta Zeolite as a

Catalyst for the Selective Reduction of Carbonyl Compounds (Meerwein-Ponndorf-Verley Reaction). *J. Am. Chem. Soc.* **2002**, *124*, 3194–3195.

(21) Corma, A.; Domine, M. E.; Valencia, S. Water-resistant solid lewis acid catalysts: Meerwein–Ponndorf–Verley and Oppenauer reactions catalyzed by tin-beta zeolite. *J. Catal.* **2003**, *215*, 294–304.

(22) Bordiga, S.; Damin, A.; Bonino, F.; Ricchiardi, G.; Lamberti, C.; Zecchina, A. The Structure of the Peroxo Species in the TS-1 Catalyst as Investigated by Resonant Raman Spectroscopy. *Angew. Chem. Int. Ed.* **2002**, *41*, 4734–4737.

(23) Gordon, C. P.; Engler, H.; Tragl, A. S.; Plodinec, M.; Lunkenbein, T.; Berkessel, A.; Teles, J. H.; Parvulescu, A.-N.; Copéret, C. Efficient epoxidation over dinuclear sites in titanium silicalite-1. *Nature* **2020**, *586*, 708–713.

(24) Corma, A.; García, H. Lewis Acids as Catalysts in Oxidation Reactions: From Homogeneous to Heterogeneous Systems. *Chem. Rev.* **2002**, *102*, 3837–3892.

(25) Eimer, G. A.; Diaz, I.; Sastre, E.; Casuscelli, S. G.; Crivello, M. E.; Herrero, E. R.; Perez-Pariente, J. Mesoporous titanosilicates synthesized from TS-1 precursors with enhanced catalytic activity in the α-pinene selective oxidation. *Appl. Catal., A* **2008**, *343*, 77–86.

(26) Song, S.; Di, L.; Wu, G.; Dai, W.; Guan, N.; Li, L. Meso-Zr-Al-beta zeolite as a robust catalyst for cascade reactions in biomass valorization. *Appl. Catal., B* **2017**, *205*, 393–403.

(27) Li, H.; Fang, Z.; Luo, J.; Yang, S. Direct conversion of biomass components to the biofuel methyl levulinate catalyzed by acid-base bifunctional zirconia-zeolites. *Appl. Catal., B* **2017**, *200*, 182–191.

(28) Bare, S. R.; Kelly, S. D.; Sinkler, W.; Low, J. J.; Modica, F. S.; Valencia, S.; Corma, A.; Nemeth, L. T. Uniform Catalytic Site in Sn-β-Zeolite Determined Using X-Ray Absorption Fine Structure. *J. Am. Chem. Soc.* **2005**, *127*, 12924–12932.

(29) Lamberti, C.; Bordiga, S.; Zecchina, A.; Carati, A.; Fitch, A.; Artioli, G.; Petrini, G.; Salvalaggio, M.; Marra, G. Structural Characterization of Ti-Silicalite-1: A Synchrotron Radiation X-Ray Powder Diffraction Study. *J. Catal.* **1999**, *183*, 222–231.

(30) Kolyagin, Y. G.; Yakimov, A. V.; Tolborg, S.; Vennestrøm, P. N.; Ivanova, I. I. Tuning of Sn-BEA Reactivity by Controlling Tin Location in the BEA Framework. *J. Phys. Chem. C* **2021**, *125*, 26679–26687.

(31) Wolf, P.; Valla, M.; Núñez Zarur, F.; Comas-Vives, A.; Rossini, A. J.; Firth, C.; Kallas, H.; Lesage, A.; Emsley, L.; Copéret, C. et al. Correlating Synthetic Methods, Morphology, Atomic-Level Structure, and Catalytic Activity of Sn-β Catalysts. *ACS Catal.* **2016**, *6*, 4047–4063.

(32) Shetty, S.; Kulkarni, B. S.; Kanhere, D. G.; Goursot, A.; Pal, S. A Comparative Study of Structural, Acidic and Hydrophilic Properties of Sn-BEA with Ti-BEA Using Periodic Density Functional Theory. *J. Phys. Chem. B* **2008**, *112*, 2573–2579.

(33) Yang, G.; Pidko, E. A.; Hensen, E. J. The Mechanism of Glucose Isomerization to Fructose over Sn-BEA Zeolite: A Periodic Density Functional Theory Study. *ChemSusChem* **2013**, *6*, 1688–1696.

(34) Montejo-Valencia, B. D.; Curet-Arana, M. C. DFT Study of the Lewis Acidities and Relative Hydrothermal Stabilities of BEC and BEA Zeolites Substituted with Ti, Sn, and Ge. *J. Phys. Chem. C* **2015**, *119*, 4148–4157.

(35) Montejo-Valencia, B. D.; Salcedo-Pérez, J. L.; Curet-Arana, M. C. DFT Study of Closed and Open Sites of BEA, FAU, MFI, and BEC Zeolites Substituted with Tin and Titanium. *J. Phys. Chem. C* **2016**, *120*, 2176–2186.

(36) Yang, G.; Pidko, E. A.; Hensen, E. J. Structure, Stability, and Lewis Acidity of Mono and Double Ti, Zr, and Sn Framework Substitutions in BEA Zeolites: A Periodic Density Functional Theory Study. *J. Phys. Chem. C* **2013**, *117*, 3976–3986.

(37) Bordiga, S.; Bonino, F.; Damin, A.; Lamberti, C. Reactivity of Ti (IV) species hosted in TS-1 towards H_2O_2–H_2O solutions investigated by ab initio cluster and periodic approaches combined with experimental XANES and EXAFS data: a review and new highlights. *Phys. Chem. Chem. Phys.* **2007**, *9*, 4854–4878.

(38) Li, G.; Pidko, E. A. The Nature and Catalytic Function of Cation Sites in Zeolites: A Computational Perspective. *ChemCatChem* **2019**, *11*, 134–156.

(39) Zhu, P.; Li, H.; Riisager, A. Sn-Beta Catalyzed Transformations of Sugars—Advances in Catalyst and Applications. *Catalysts* **2022**, *12*, 405.

(40) To, J.; Sokol, A. A.; French, S. A.; Catlow, R. A.; Sherwood, P.; van Dam, H. J. J. Formation of heteroatom acitve sites in zeolites by hydrolysis and inversion. *Angew. Chem. Int. Ed.* **2006**, *45*, 1633–1638.

(41) Geobaldo, F.; Bordiga, S.; Zecchina, A.; Giamello, E. DRS UV-Vis EPR spectroscopy of hydroperoxo and superoxo complexes in titanium silicalite. *Catal. Lett.* **1992**, *16*, 109–115.

(42) Sacrano, D.; Zecchnia, A.; Bordiga, S.; Geobaldo, F.; Spoto, G.; Petrini, G.; Leofanti, G.; Padovan, M.; Tozzola, G. Fourier-transform infrared and Raman spectra of pure and Al-, B-, Ti- and Fe- substituted silicalites: stretching-mode region. *J. Chem. Soc. Faraday Trans.* **1993**, *89*, 4123–4130.

(43) Josephson, T. R.; Jenness, G. R.; Vlachos, D. G.; Caratzoulas, S. Distribution of open sites in Sn-Beta zeolite. *Microporous Mesoporous Mater.* **2017**, *245*, 45–50.

(44) Bukowski, B.; Bates, J.; Gounder, R.; Greeley, J. First principles, microkinetic, and experimental analysis of Lewis acid site speciation during ethanol dehydration on Sn-Beta zeolites. *J. Catal.* **2018**, *365*, 261–276.

(45) Xu, J.; Wang, Q.; Deng, F. Metal Active Sites and Their Catalytic Functions in Zeolites: Insights from Solid-State NMR Spectroscopy. *Acc. Chem. Res.* **2019**, *52*, 2179–2189.

(46) Wolf, P.; Valla, M.; Rossini, A. J.; Comas-Vives, A.; Núñez-Zarur, F.; Malaman, B.; Lesage, A.; Emsley, L.; Copéret, C.; Hermans, I. NMR Signatures of the Active Sites in Sn-β Zeolite. *Angew. Chem.* **2014**, *126*, 10343–10347.

(47) Kolyagin, Y. G.; Yakimov, A. V.; Zasukhin, D. S.; Ivanova, I. I. Direct Identification of Zeolite Beta Polymorphs by Solid-State ^{29}Si Nuclear Magnetic Resonance Spectroscopy. *J. Phys. Chem. Lett.* **2022**, *13*, 10793–10798.

(48) Wang, W.; Xu, J.; Deng, F. Recent advances in solid-state NMR of zeolite catalysts. *Nat. Sci. Rev.* **2022**, *9*, nwac155.

(49) Newsam, J.; Treacy, M.; Koetsier, W.; Gruyter, C. d. Structural characterization of zeolite beta. *Proc. R. Soc. London A* **1988**, *420*, 375–405.

(50) Pace, R. B.; Lardinois, T. M.; Ji, Y.; Gounder, R.; Heintz, O.; Crocker, M. Effects of Treatment Conditions on Pd Speciation in CHA and Beta Zeolites for Passive NO_x Adsorption. *ACS Omega* **2021**, *6*, 29471–29482.

(51) Bukowski, B. C.; Bates, J. S.; Gounder, R.; Greeley, J. Defect-Mediated Ordering of Condensed Water Structures in Microporous Zeolites. *Angew. Chem. Int. Ed.* **2019**, *58*, 16422–16426.

(52) Bols, M. L.; Snyder, B. E.; Rhoda, H. M.; Cnudde, P.; Fayad, G.; Schoonheydt, R. A.; Van Speybroeck, V.; Solomon, E. I.; Sels, B. F. Coordination and activation of nitrous oxide by iron zeolites. *Nat. Catal.* **2021**, *4*, 332–340.

(53) Dai, W.; Lei, Q.; Wu, G.; Guan, N.; Hunger, M.; Li, L. Spectroscopic Signature of Lewis Acidic Framework and Extraframework Sn Sites in Beta Zeolites. *ACS Catal.* **2020**, *10*, 14135–14146.

(54) Yang, X.; Lv, B.; Lu, T.; Su, Y.; Zhou, L. Promotion effect of Mg on a post-synthesized Sn-Beta zeolite for the conversion of glucose to methyl lactate. *Catal. Sci. Technol.* **2020**, *10*, 700–709.

(55) Joshi, H.; Ochoa-Hernández, C.; Nürenberg, E.; Kang, L.; Wang, F. R.; Weidenthaler, C.; Schmidt, W.; Schüth, F. Insights into the mechanochemical synthesis of Sn-β: Solid-state metal incorporation in beta zeolite. *Microporous Mesoporous Mater.* **2020**, *309*, 110566.

(56) Kim, Y.-S.; Cho, K.-S.; Lee, Y.-K. Structure and Activity of Ni2P/Desilicated Zeolite β Catalysts for Hydrocracking of Pyrolysis Fuel Oil into Benzene, Toluene, and Xylene. *Catalysts* **2020**, *10*, 47.

(57) Qi, G.; Wang, Q.; Xu, J.; Wu, Q.; Wang, C.; Zhao, X.; Meng, X.; Xiao, F.; Deng, F. Direct observation of tin sites and their reversible interconversion in zeolites by solid-state NMR spectroscopy. *Commun. Chem.* **2018**, *1*, 22.

(58) Jansen, J. C.; Creyghton, E. J.; Njo, S. L.; van Koningsveld, H.; van Bekkum, H. On the remarkable behaviour of zeolite Beta in acid catalysis. *Catal. Today* **1997**, *38*, 205–212.

(59) He, Z.; Wu, J.; Gao, B.; He, H. Hydrothermal Synthesis and Characterization of Aluminum-Free Mn-β Zeolite: A Catalyst for Phenol Hydroxylation. *ACS Appl. Mater. Interfaces* **2015**, *7*, 2424–2432.

(60) Peeters, E.; Calderon-Ardila, S.; Hermans, I.; Dusselier, M.; Sels, B. F. Toward Industrially Relevant Sn-BETA Zeolites: Synthesis, Activity, Stability, and Regeneration. *ACS Catal.* **2022**, *12*, 9559–9569.

(61) Jon, H.; Lu, B.; Oumi, Y.; Itabashi, K.; Sano, T. Synthesis and thermal stability of beta zeolite using ammonium fluoride. *Microporous Mesoporous Mater.* **2006**, *89*, 88–95.

(62) Kresse, G.; Furthmüller, J. Efficiency of ab-initio total energy calculations for metals and semiconductors using a plane-wave basis set. *Comput. Mater. Sci.* **1996**, *6*, 15–50.

(63) Kresse, G.; Hafner, J. Ab initio molecular-dynamics simulation of the liquid-metal–amorphous-semiconductor transition in germanium. *Phys. Rev. B* **1994**, *49*, 14251.

(64) Blöchl, P. E. Projector augmented-wave method. *Phys. Rev. B* **1994**, *50*, 17953.

(65) Kresse, G.; Joubert, D. From ultrasoft pseudopotentials to the projector augmented-wave method. *Phys. Rev. B* **1999**, *59*, 1758.

(66) Perdew, J. P.; Burke, K.; Ernzerhof, M. Generalized Gradient Approximation Made Simple. *Phys. Rev. Lett.* **1996**, *77*, 3865.

(67) Grimme, S. Semiempirical GGA-type density functional constructed with a long-range dispersion correction. *J. Comput. Chem.* **2006**, *27*, 1787–1799.

(68) Higgins, J.; LaPierre, R.; Schlenker, J.; Rohrman, A.; Wood, J.; Kerr, G.; Rohrbaugh, W. The framework topology of zeolite beta. *Zeolites* **1988**, *8*, 446–452.

(69) Lu, T.; Yan, W.; Xu, R. Chiral zeolite beta: structure, synthesis, and application. *Inorg. Chem. Front.* **2019**, *6*, 1938–1951.

(70) Tang, L.; Shi, L.; Bonneau, C.; Sun, J.; Yue, H.; Ojuva, A.; Lee, B.-L.; Kritikos, M.; Bell, R. G.; Bacsik, Z. et al. A zeolite family with chiral and achiral structures built from the same building layer. *Nat. Mater.* **2008**, *7*, 381–385.

(71) Corma, A.; Moliner, M.; Cantín, Á.; Díaz-Cabañas, M. J.; Jordá, J. L.; Zhang, D.; Sun, J.; Jansson, K.; Hovmöller, S.; Zou, X. Synthesis and Structure of Polymorph B of Zeolite Beta. *Chem. Mater.* **2008**, *20*, 3218–3223.

(72) International Zeolite Association `http://www.iza-structure.org/databases/`, (accessed: April 23, 2024).

(73) Hayek, E. E.; Harbuzaru, B.; Martens, J.; Chizallet, C. Ab initio investigation of the relative stability of silicogermanates and their (Alumino)Silicates counterparts. *Microporous Mesoporous Mater.* **2020**, *306*, 110425.

(74) Henkelman, G.; Arnaldsson, A.; Jónsson, H. A fast and robust algorithm for Bader decomposition of charge density. *Comput. Mater. Sci. 36*, 354–360.

(75) Sanville, E.; Kenny, S.; Smith, R.; Henkelman, G. Improved grid-based algorithm for Bader charge allocation. *J. Comput. Chem. 28*, 899–908.

(76) Leydier, F.; Chizallet, C.; Costa, D.; Raybaud, P. CO adsorption on amorphous silica–alumina: electrostatic or Brønsted acidity probe? *Chem. Commun.* **2012**, *48*, 4076–4078.

(77) Leydier, F.; Chizallet, C.; Costa, D.; Raybaud, P. Revisiting carbenium chemistry on amorphous silica-alumina: Unraveling their milder acidity as compared to zeolites. *J. Catal.* **2015**, *325*, 35–47.

(78) Silaghi, M.-C.; Chizallet, C.; Sauer, J.; Raybaud, P. Dealumination mechanisms of zeolites and extra-framework aluminum confinement. *J. Catal.* **2016**, *339*, 242–255.

(79) Goyal, A.; Agarwal, V. Rate-Enhancing Role of Water in H-BEA and Sn-BEA for Keto–Enol Tautomerization of Acetone: A DFT Study. *J. Phys. Chem. C* **2023**, *127*, 22618–22628.

(80) Henkelman, G.; Arnaldsson, A.; Jónsson, H. A fast and robust algorithm for Bader decomposition of charge density. *Comput. Mater. Sci.* **2006**, *36*, 354–360.

(81) Sanville, E.; Kenny, S.; Smith, R.; Henkelman, G. Improved grid-based algorithm for Bader charge allocation. *J. Comput. Chem.* **2007**, *28*, 899–908.

(82) Tang, W.; Sanville, E.; Henkelman, G. A grid-based Bader analysis algorithm without lattice bias. *J. Phys. Condens. Matter* **2009**, *21*, 084204.

(83) Choudhuri, I.; Truhlar, D. Calculating and Characterizing the Charge Distributions in Solids. *J. Chem. Theory Comput.* **2020**, *16*, 5884–5892.

(84) Ertl, G.; Knözinger, H.; Weitkamp, J. *Handbook of Heterogeneous Catalysis*; VCH Weinheim, 1997; Vol. 2.

(85) Knözinger, H. Infrared Spectroscopy for the Characterization of Surface Acidity and Basicity. *Handbook of Heterogeneous Catalysis: Online* **2008**, 1135–1163.

(86) Treps, L.; Gomez, A.; de Bruin, T.; Chizallet, C. Environment, Stability and Acidity of External Surface Sites of Silicalite-1 and ZSM-5 Micro and Nano Slabs, Sheets, and Crystals. *ACS Catal.* **2020**, *10*, 3297–3312.

(87) Thibault-Starzyk, F.; Stan, I.; Abelló, S.; Bonilla, A.; Thomas, K.; Fernandez, C.; Gilson, J.-P.; Pérez-Ramírez, J. Quantification of enhanced acid site accessibility in hierarchical zeolites – The accessibility index. *J. Catal.* **2009**, *264*, 11–14.

(88) Dijkmans, J.; Gabriëls, D.; Dusselier, M.; Clippel, F. D.; Vanelderen, P.; Houthoofd, K.; Malfliet, A.; Pontikes, Y.; Sels, B. Productive sugar isomerization with highly active Sn in dealuminated β-zeolites. *Green Chem.* **2013**, *15*, 2777–2785.

(89) Dijkmans, J.; Dusselier, M.; Gabriëls, D.; Houthoofd, K.; Magusin, P.; Huang, S.; Pontikes, Y.; Trekels, M.; Vantomme, A.; Giebeler, L. et al. Cooperative Catalysis for Multistep Biomass Conversion with Sn/Al Beta Zeolite. *ACS Catal.* **2015**, *5*, 928–940.

(90) Tang, B.; Dai, W.; Wu, G.; Guan, N.; Li, L.; Hunger, M. Improved Postsynthesis Strategy to Sn-Beta Zeolites as Lewis Acid Catalysts for the Ring-Opening Hydration of Epoxides. *ACS Catal.* **2014**, *4*, 2801–2810.

(91) Kulkarni, B.; Krishnamurty, S.; Pal, S. Probing Lewis acidity and reactivity of Sn- and Ti-beta zeolite using industrially important moieties: A periodic density functional study. *J. Mol. Catal. A: Chem.* **2010**, *329*, 36–43.

TOC Graphic

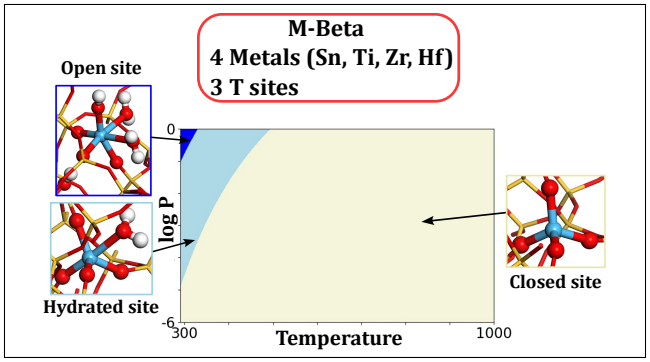
M-Beta
4 Metals (Sn, Ti, Zr, Hf)
3 T sites
Open site
Hydrated site
Closed site
log P
0
-6
300
1000
Temperature